Numerical evaluation of the thermal performance of different types of double glazing flat-plate solar air collectors

Chen, C.Q.; Diao, Y.H.; Zhao, Y.H.; Wang, Z.Y.; Zhu, T.T.; Wang, T.Y.; Liang, L.

Published in:
Energy

Link to article, DOI:
10.1016/j.energy.2021.121087

Publication date:
2021

Document Version
Peer reviewed version

Journal Pre-proof

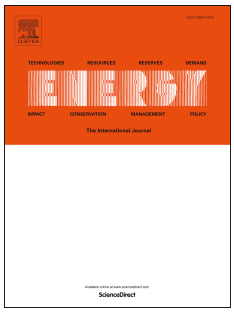

Numerical evaluation of the thermal performance of different types of double glazing flat-plate solar air collectors

C.Q. Chen, Y.H. Diao, Y.H. Zhao, Z.Y. Wang, T.T. Zhu, T.Y. Wang, L. Liang

PII: S0360-5442(21)01335-9

DOI: https://doi.org/10.1016/j.energy.2021.121087

Reference: EGY 121087

To appear in: *Energy*

Received Date: 21 December 2020

Revised Date: 20 April 2021

Accepted Date: 26 May 2021

Please cite this article as: Chen CQ, Diao YH, Zhao YH, Wang ZY, Zhu TT, Wang TY, Liang L, Numerical evaluation of the thermal performance of different types of double glazing flat-plate solar air collectors, *Energy*, https://doi.org/10.1016/j.energy.2021.121087.

C. Q. Chen: Conceptualization, Methodology, Software, Formal analysis, Investigation, Data Curation, Writing - Original Draft, Writing - Review & Editing

Y. H. Diao: Conceptualization, Methodology, Formal analysis, Resources, Writing - Review & Editing, Supervision

Y. H. Zhao: Resources, Supervision

Z. Y. Wang: Validation

T. T. Zhu: Conceptualization, Methodology

T.Y. Wang: Formal analysis

L. Liang: Data Curation, Formal analysis

Numerical evaluation of the thermal performance of different types of double glazing flat-plate solar air collectors

C.Q. Chen [a], Y.H. Diao [a*], Y.H. Zhao [a], Z.Y. Wang [a], T.T. Zhu [b, c], T.Y. Wang [a], L. Liang [a]

a. Beijing Key Laboratory of Green Built Environment and Efficient Technology, Beijing University of Technology, Beijing 100124, China

b. Tianjin Key Lab of Refrigeration Technology, Tianjin University of Commerce, No.409 Guangrong Road, Beichen District, Tianjin 300134, China

c. Department of Mechanical Engineering, Technical University of Denmark, Nils Koppels Allé, Building 403, 2800, Kongens Lyngby, Denmark

Abstract

As the main source of heat loss of flat-plate solar air collectors (FPSACs), single glazing cover reduces the thermal performance of FPSAC. This situation becomes serious when the ambient temperature is low or the inlet temperature is high. A double glass cover with good thermal insulation is a good solution. This work aims to investigate the thermal performance of double glazing FPSAC at low ambient temperature and high inlet temperature. The thermal performance of four FPSACs with single glazing (Model 1), double glazing filled with air (Model 2), double glazing filled with argon (Model 3), and vacuum glazing (Model 4) as the glass cover at different ambient temperatures, different heat transfer Air (HTA) inlet temperatures, and different HTA volume flow rates are studied and compared. Result demonstrates that Models 2, 3, and 4 have better thermal performance at low ambient temperature and high inlet temperature compared with Model 1. When the inlet temperature is 65 °C and ambient temperature is −10 °C, the thermal efficiencies of Models 2, 3, and 4 are 1.65, 1.72, and 2.29 times higher than that of Model 1, respectively. The efficiency factor and total heat loss coefficient of Model 4 are 0.62707 and 2.21745,

* Corresponding author. Tel: +86 010 67391608-802; fax: +86 010 67391608-802
E-mail address: diaoyanhua@bjut.edu.cn (Y.H. Diao)

respectively.

Keywords: Flat-plate solar air collector; Double glazing; Vacuum glazing; Numerical simulation

Nomenclature		ω	Permeability factor
FPSAC	Flat-plate solar air collector	$\bar{\bar{\tau}}$	Stress tensor (N/m^2)
FPSC	Flat-plate solar collector	ε	Emissivity
HTA	Heat transfer air	γ	Transmissivity
Dimensional variables		χ	Porosity of the porous medium
A	Area (m^2)	λ	Thermal conductivity (W/(m·K))
C_2	Inertial resistance factor	Ω'	Solid angle
C_p	Specific heat capacity (J/kg·°C)	Ψ	Function of the view factor
E_f	Enthalpy (kJ/kg)	η_0	Optical efficiency
$\vec{g}$	Gravity acceleration (m/s^2)	η	Efficiency
h	Heat transfer coefficient (W/(m^2·K))	θ	Installation angle (°)
I	Radiation intensity (W/m^2)		
J_i	Diffusion flux of component i	**Subscripts**	
M	Molar mass	*amb*	Ambient
n	Refractive index	*ac*	Air channel
Δn	Thickness of the porous medium	*av*	Average
ρ	Density (kg/m^3)	*abs*	Absorber
P	Pressure (Pa)	*bp*	Back plate
R	Thermal resistance (K/W)	*con*	Convection
R'	Constant (approximately 8.314 J/(mol·K))	*coll*	Collector
Q	Power (W)	*eff*/*e*	Effective
$\vec{r}$	Position vector	*f*	Fluid
s	Length along the way	*g*	Glass
$\vec{s}$	Direction vector	*HTA*	Heat transfer air

$\dot{s}'''$	Heat dissipation	*htc*	Heat transfer channel
T	Temperature (°C)	*in*	Inlet
T_m	Average temperature of HTA	*ins*	Insulation
ΔT	Temperature difference (°C)	*loss*	Loss
U_L	Total heat loss coefficient of collector	*out*	Outlet
μ	Viscosity (kg/(m·s))	*r*	Radiation
α	Absorptivity	*s*	Solid
β	Thermal expansion coefficient (1/K)	*sky*	Sky
σ	Stefan Boltzmann constant	*va*	Vacuum
σ_s	Scattering coefficient (1/m)	*ws*	Wind speed (m/s)
$\vec{v}$	Velocity (m/s)	*0*	Reference
Φ	Phase function		

1. Introduction

With the increasing demand for fossil energy, the problem of energy shortages has become increasingly urgent. The development of renewable clean energy technology has been increasingly concerned by most countries, especially considering the environmental pollution and the greenhouse effect caused by the massive consumption of fossil energy [1]. Solar energy, which is characterized with wide distribution, cleanliness, and free, is widely researched and utilized.

At present, the utilization of solar energy is mainly divided into photovoltaic and photothermal. Scientists have been constantly trying to promote the use of photovoltaics by improving photoelectric conversion efficiency and reducing costs. In medium and high temperatures, solar thermal power generation technology is a main research direction. In medium and low temperatures, photothermal technology is closely integrated with domestic hot water, seawater desalination, crop drying, and building heating. Among the many types of solar collectors, flat-plate solar collectors (FPSCs) have been widely studied by scholars due to their low investment, low

maintenance cost, and no need for solar tracking systems [2]. Thus, various new technologies are used to improve the thermal performance of FPSCs. The FPSC is represented by discrete temperature nodes connected with thermal resistances, as displayed in **Fig. 1**. In summary, the research ideas for improving the performance of FPSCs can be summarized in the following five aspects.

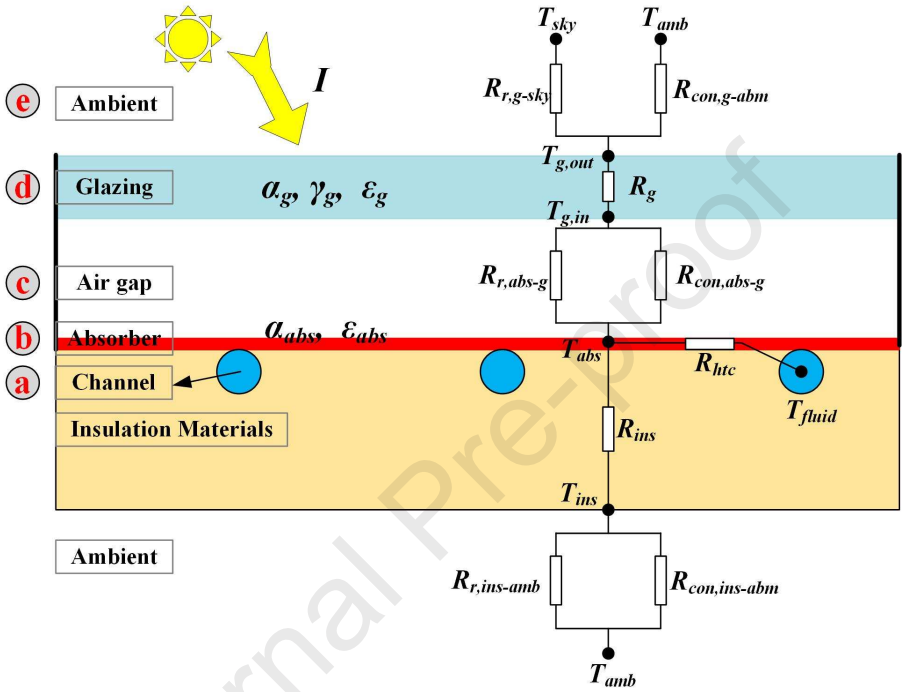

Fig. 1 Schematic of a heat transfer model of traditional FPSC

a. For heat transfer fluid, enhance the heat exchange between heat transfer fluid and absorber.

Reduce the heat transfer resistance on the heat transfer channels (R_{htc}). Innovative methods, such as using nanofluids [3, 4], optimizing the structure of heat exchange channels [5, 6], and using high thermal conductivity element-heat pipes [7, 8], have been studied by researchers.

b. For absorber, increase absorptivity (α_{abs}) while reducing emissivity (ε_{abs}).

Increase the absorption of solar energy and the radiation heat transfer resistance between the absorber and the glazing ($R_{r,abs\text{-}g}$). Absorbers characterized with high absorptivity and low emissivity have been developed [9, 10], and the absorber cost, roughness, and durability have been considered by scholars [11].

c. For air gap, reduce the heat exchange rate between the absorber and the glazing.

Increase the convection heat transfer resistance between the absorber and the glazing ($R_{con,abs\text{-}g}$). Many studies are conducted on the influence of air gap thickness on the thermal performance of FPSCs [12, 13].

d. For glazing, increase the amount of solar radiation penetrating the glazing and reduce its heat loss to the ambient and the sky.

Increase the transmissivity of the glazing (γ_g) and the heat transfer resistance between the glazing and the ambient or sky ($R_{con,g\text{-}amb}$ or $R_{r,g\text{-}sky}$). Many interesting technical means, such as coatings with low emissivity and high transmissivity, are attached on the glass surface to increase the radiant heat transfer resistance ($R_{r,g\text{-}sky}$) [14, 15]. Multiple layers of glazing are used to reduce the temperature difference between the glazing and the ambient ($T_g - T_{amb}$) [16, 17]. Different glazing thicknesses are used to balance the thermal conductivity resistance (R_g) and transmissivity (γ_g) of the glass [18].

e. For solar, increase the solar radiation density projected on the glazing (I),

Concentrators and mirrors are main the technology used by researchers [19, 20].

The five research ideas improve the thermal performance of FPSCs to varying degrees. Increasing studies have found that the main heat loss of FPSCs comes from the top glazing (larger than 75% of the total input solar energy in some cases) [2, 12, 14, 17, 18]. In particular, when the FPSC is connected to the user/target, the heat loss of the top glazing reaches an unacceptable level. This situation becomes serious when the ambient temperature is relatively low [21–23]. The low efficiency and high heat loss characteristics limit the application of FPSC [17]. Carmonna [21] tested the thermal performance of an FPSC with latent thermal storage through experiment. The research results show that the top glazing temperature of FPSC is always higher than its outlet temperature, especially when RT60 is used as the phase change material. This phenomenon causes a large heat loss of the top glazing. Kabeel [22] examined two collector-storage solar heating systems for desalination through experiment. The

research results on phase change material as thermal storage medium show that the temperature of the top glazing is approximately 20 °C higher than the ambient temperature on average during the day. This phenomenon causes huge heat loss of the top glazing. In particular, Chen [23] evaluated the performance of a closed collector-storage solar air heating system with latent thermal storage through experiment. The study results show that the heat loss from the top glazing in summer and winter accounts for 36.67% and 51.40% of the total input solar radiation, respectively, which is 1.49–2.82 times higher than the energy stored in the phase change material.

Improving the thermal performance of FPSCs at low ambient temperature and high inlet temperature is a technical challenge that must be overcome to expand their application range. The direct method is to reduce the heat loss of the top glazing [18, 23]. Hollow and vacuum glazings (double glazing) are widely used in buildings to reduce the heat loss of windows. The good insulation properties of hollow and vacuum glazings can greatly reduce the heat loss of buildings, and numerous research results show that this design is effective [24, 25]. Applying hollow glazing (air or argon filled in double glazing) and vacuum glazing to FPSCs to reduce the heat loss at the top is worth exploring. The application of double glazing in FPSCs has been partially studied, and good results have been achieved. However, to the best of our knowledge, the deficiencies of these studies are as follows:

1. The performance of FPSCs with double glazing at high inlet temperatures and low ambient temperatures has not been fully studied. In some special occasions, such as collector-storage solar heating system (>$T_{melting}$) and seawater desalination (> 50 °C), a high inlet temperature is necessary to fully melt the phase change material or meet the temperature of production technology [26]. In northern China, the average ambient temperature in January is as low as −10 °C–−20 °C [27]. The application area of FPSC can be expanded if it can work efficiently in a low-temperature environment.

2. Studies on hollow and vacuum glazings in FPSCs where air as the heat transfer fluid are scarce. The low thermal conductivity of air causes an FPSC to use

air as the heat transfer fluid to have lower thermal performance than that using water as the heat transfer fluid with a similar configuration. However, FPSACs have great application potential in agriculture, textiles, desalination, and construction [23]. Existing research on double glazing FPSAC mainly uses the gap between two glasses as HTA pass channels rather than a closed space. This method causes the insulation performance of the glass cover with double glazing to decrease when the inlet temperature rises.

Four FPSAC numerical models, namely, single glazing FPSAC, hollow glazing filled with air FPSAC, hollow glazing filled with argon FPSAC, and vacuum glazing FPSAC, are established and investigated in the current study to supplement the above research gaps. A single glazing FPSAC is built to verify the reliability of the numerical model. Subsequently, the thermal performance of the four FPSACs under different inlet temperatures (35 °C–60 °C), different ambient temperatures (−20 °C–40 °C), and different HTA volumetric flow rates (30–210 m^3/h) is studied and compared. The normalized efficiency curves of the four models are evaluated and compared.

2 Experimental and numerical model development

2.1 Experimental setup

As shown in **Fig. 2**, the FPSAC is mainly composed of glass cover (ultra white glass), absorber, FMHPAs, air channel, louver fins, and thermal insulation material (extruded board and rubber insulation cotton). As a high thermal conductivity element, the FMHPA transfers heat from the absorber to the air channel. The specific structural parameters of FPSAC are shown in **Table 1**.

As shown in **Fig. 3**, the experimental test system is mainly composed of the following parts.

1. An FPSAC is used to convert solar energy into thermal energy, and part of the heat is taken away by the HTA.

2. An HTA control module mainly consists of a water–air heat exchanger, a flowmeter, an air valve, a fan and a water bath. The air valve and the water–air heat

exchanger control the volume flow rate and inlet temperature of the HTA, respectively.

3. A data acquisition module is mainly composed of thermocouple, computer, and data taker (Agilent data collector). The temperatures of the inlet, outlet, absorber, glass cover and back plate of FPSAC are collected in real time. The temperature monitoring point arrangement of the FPSAC is already introduced in Fig. 7 of Ref. **[23]**. This study will not be listed in detail.

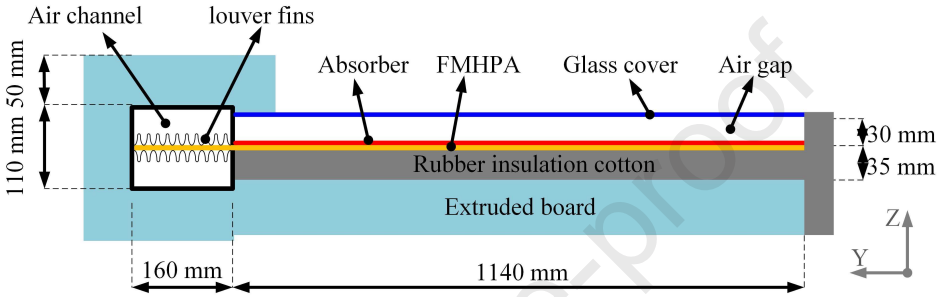

(A) Cross sectional view of FPSAC

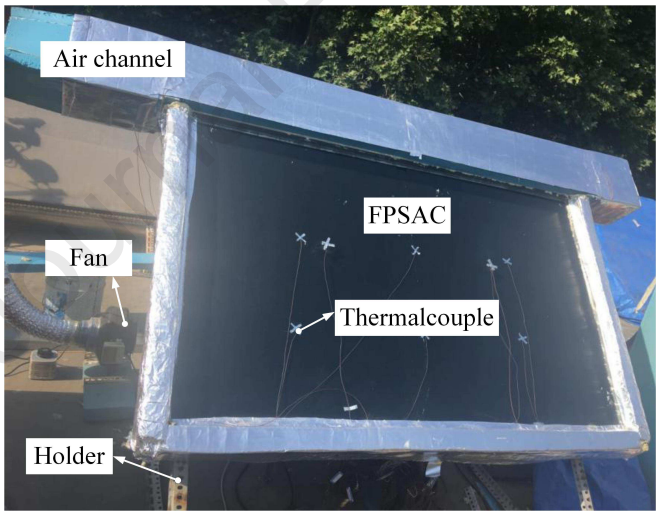

(B) Physical map of FPSAC

Fig. 2 Cross sectional and physical map of FPSAC

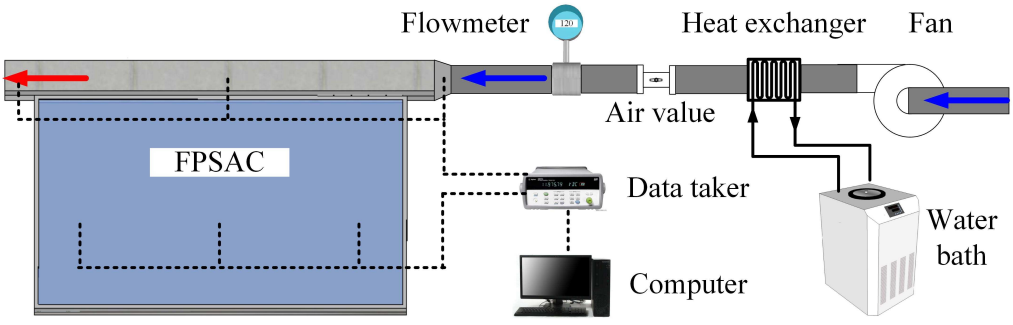

Fig. 3 Schematic of the experimental system

Table 1 Specific structural parameters of FPSAC

Element	Dimension
Louver fin height	8 mm
Louver fin width	80 mm
Louver fin spacing	4 mm
Glazing	1140 mm × 1700 mm × 3 mm
Absorber	1100 mm × 1545 mm × 0.3 mm
FMHPA (21 pieces)	1300 mm × 80 mm × 3 mm

The physical parameters of the materials of each component of FPSAC are shown in **Table 2**. The optical properties of the related materials are presented in **Table 3**.

Table 2 Physical parameters of the materials of each component

Item	ρ (kg/m^3)	C_p (J/(kg·K))	λ (W/(m·K))	μ (kg/(m·s))
Porous medium	2719	871	155	-
Air	Boussinesq	1005	0.02826	19.6×10^{-6}
FMHPA	900	600	45,000 [32]	-
Rubber cotton	50	1500	0.034	-
Extruded board	30	1500	0.027	-
Absorber	7850	460	15	-
Glazing	2220	730	0.8	-
Argon	1.6228	520.64	0.0158	21.25×10^{-6}
Vacuum [33]	1.08×10^{-4}	1017	0.02750	0.1926

Table 3 Optical properties of related materials

Item	Absorptivity/α	Transmissivity/γ	Reflectivity	Emissivity/ε
Absorber	0.93	0	0.07	0.08
Glazing	0.01	0.90	0.09	0.85

2.2 Numerical model assumptions and governing equations

ANSYS Fluent 17.0 provides a wealth of mathematical calculation models, including energy equation, viscous model, and radiation model. As a reliable and convenient numerical simulation solver, it is widely used in the optimization research of solar collectors [28, 29]. In this work, the commercial steady state ANSYS Fluent 17.0 was selected for numerical simulation. The following assumptions are given to the numerical model before verifying its reliability.

a. The louver fin is schematized as a porous medium in the numerical calculation because this research mainly focuses on the glass cover side of FPSAC. The complex pore structure of louver fin is disregarded, but the flow and heat transfer characteristics are considered. The reliability of this assumption has been recognized [30].

b. The FMHPA is schematized as a good conductor without considering the evaporation and condensation of its internal working fluid. Related studies have shown that the equivalent thermal conductivity of FMHPA can reach the order of 10^4 [31, 32], which is larger than the thermal conductivity of air and other components of the collector. This condition indicates that small changes in the heat transfer performance of FMHPA does not have a substantial effect on the heat transfer of FPSAC because the heat transfer resistance of FPSAC is not on the FMHPA side.

c. The thermal conductivity, specific heat capacity, and viscosity of the air are constant, except for density.

The governing equations described by FPSAC's heat transfer and flow are as follows:

Continuity equation

$$\nabla \cdot \vec{v} = 0, \tag{1}$$

Momentum equation

$$\left(\rho \vec{v} \cdot \nabla\right) \vec{v} = \rho \vec{g} - \nabla P + \nabla \bar{\bar{\tau}} + \vec{S}_i, \tag{2}$$

where $\vec{v}$ is the velocity, m/s, ρ is the air density in the buoyancy term (kg/m^3), $\vec{g}$ is the gravitational acceleration (m/s^2), P is the pressure (Pa), and $\bar{\bar{\tau}}$ is the stress tensor

(N/m^2).

In the buoyancy term of the momentum equation, the air density can be considered to satisfy the Boussinesq approximation, whereas the air density is considered constant in other equations, that is,

$$\rho = \rho_0\left[1 - \beta\left(T - T_0\right)\right], \tag{3}$$

where ρ_0 is the constant density of the air (kg/m^3), β is the thermal expansion coefficient (1/K), and T_0 is the reference temperature (°C).

The source term $\vec{S}_i$ in the momentum equation is modeled to the pressure drop in the porous medium (louver fin) and is composed of two parts: a viscous loss term and an inertial loss term [30].

$$\vec{S}_i = -\left(\frac{\mu}{\omega}v_i + \frac{1}{2}C_2\rho\left|v_j\right|v_j\right), \tag{4}$$

where ω and C_2 are the permeability and inertial resistance factors, respectively. Viscous and inertial resistance need to be defined/calculated before the calculation starts.

According to [23], louver fin's pressure–volume flow rate curve (experimental data) is measured and fitted as follows:

$$\Delta P = ax + bx^2 = 3.301v + 1.962v^2, \tag{5}$$

where the inertial resistance and viscous resistance factors can be calculated using coefficients *a* and *b* in Eqs. (6) and (7) [30].

$$a = \frac{\mu}{\omega}\Delta n \rightarrow \frac{1}{\omega} = \frac{a}{\mu \cdot \Delta n}, \tag{6}$$

$$b = \frac{1}{2}C_2\rho\Delta n \rightarrow C_2 = \frac{2b}{\rho \cdot \Delta n}. \tag{7}$$

where μ is the air viscosity ($kg/(m\cdot s)$), and Δn is the thickness of the porous medium (0.008 m).

Energy equation [30]

$$\nabla \cdot \left[\vec{v} \left(\rho_f E_f + p \right) \right] = \nabla \cdot \left[\lambda_{eff} \nabla T - \left(\sum_i h_i J_i \right) + \left(\bar{\bar{\tau}} \cdot \vec{v} \right) \right] + S_f^h , \quad (8)$$

where E_f is the enthalpy of fluid (kJ/kg), J_i is the diffusion flux of component i, S_f^h is the volume heat source term, λ_{eff} is the effective thermal conductivity, and the calculation method is as follows:

$$\lambda_{eff} = \chi \lambda_f + (1 - \chi) \lambda_s . \quad (9)$$

where λ_f and λ_s are the fluid phase and solid phase thermal conductivities, respectively, and χ is the porosity of the porous medium (0.93).

The discrete ordinates radiation model is used to simulate solar radiation and calculate the radiative heat transfer of each surface. The transport equation of its radiation intensity in space coordinates is as follows [32]:

$$\nabla \cdot \left[I\left(\vec{r}, \vec{s}\right) \vec{s} \right] + \left(\alpha' + \sigma_s \right) I\left(\vec{r}, \vec{s}\right) = \alpha' n^2 \frac{\sigma T^4}{\pi} + \frac{\sigma_s}{4\pi} \int_0^{4\pi} I\left(\vec{r}, \vec{s}\right) \Phi\left(\vec{s}, \vec{s}'\right) d\Omega , \quad (10)$$

where $\vec{r}$, $\vec{s}$, and $\vec{s}'$ are the position vector, direction vector, and heat dissipation direction, respectively, s is the length along the way, α' is the absorption coefficient (1/m), n is the refractive index, σ_s is the scattering coefficient (1/m), I is the radiation intensity (W/m^2), Φ is the phase function, and Ω' is the solid angle.

2.3 Numerical model and grid division

The preprocessing commercial software Gambit 2.4.6 is used to perform tasks, such as modeling, meshing, and defining boundary/region types. **Figs. 4** and **5** demonstrate the numerical model and meshing diagrams of FPSAC, respectively. The size ratio of the numerical model and the original model is 1:1. In view of the regular geometric structure of each component of FPSAC, the structured grids are generated with Gambit tool. The boundary layer grid is generated at the boundary of the glass cover and absorber.

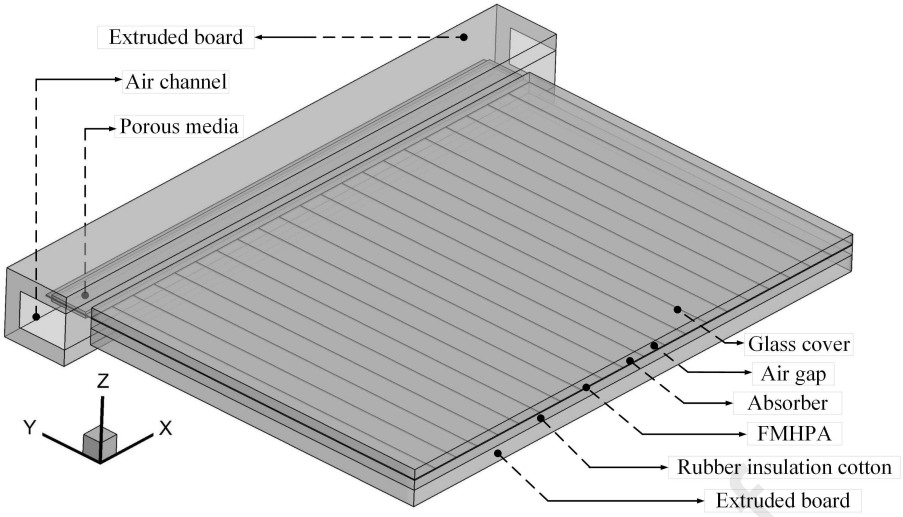

Fig. 4 Model diagram of the FPSAC

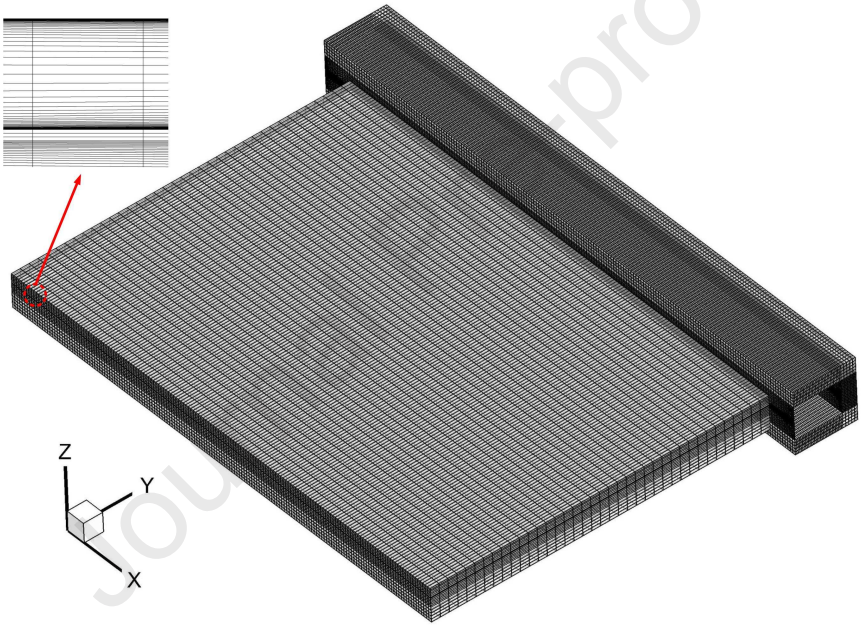

Fig. 5 Mesh diagram of the FPSAC

2.4 Boundary conditions and materials

The top glazing is set as a mix boundary. The heat loss of convective heat transfer with the ambient ($Q_{con,g\text{-}amb}$) and the heat loss of radiation heat transfer with the sky ($Q_{r,g\text{-}sky}$) are considered. The type of glass is ultra white glass with a thickness of 3 mm. The air channel and back plan are part of the FPSAC heat loss source, and the convective heat transfer between them and the ambient are considered ($Q_{ac\text{-}amb}$ and $Q_{bp\text{-}amb}$). Their outer surface temperature differs slightly from the ambient temperature because the air duct and the back plate have good insulation measures; thus, the

radiation heat transfer losses between them and ambient can be ignored [17].

The convective heat transfer coefficient between the glass cover (top glazing), air channel, back plate, and the ambient is determined using **Eq. (11)** [9].

$$h_{con,g\text{-}amb}=h_{ac\text{-}amb}=h_{bp\text{-}amb}=2.9v_{ws}+4.3, \quad (11)$$

The radiation heat transfer loss between the glass cover and the sky is a nonnegligible source of loss. The sky is treated as a blackbody, and the equivalent blackbody temperature (T_{sky}^{*}) is calculated as follows [9]:

$$T_{sky}^{*}=\left[\psi\cdot\left(T_{sky}+273.15\right)^{4}+\left(1-\psi\right)\cdot\left(T_{amb}+273.15\right)^{4}\right]^{0.25}-273.15, \quad (12)$$

$$T_{sky}=T_{amb}-0.015\cdot I, \quad (13)$$

$$\psi=0.5\cdot\left(1+\cos\theta\right), \quad (14)$$

where ψ is a function of the view factor, and θ is the installation angle of FPSAC (45°).

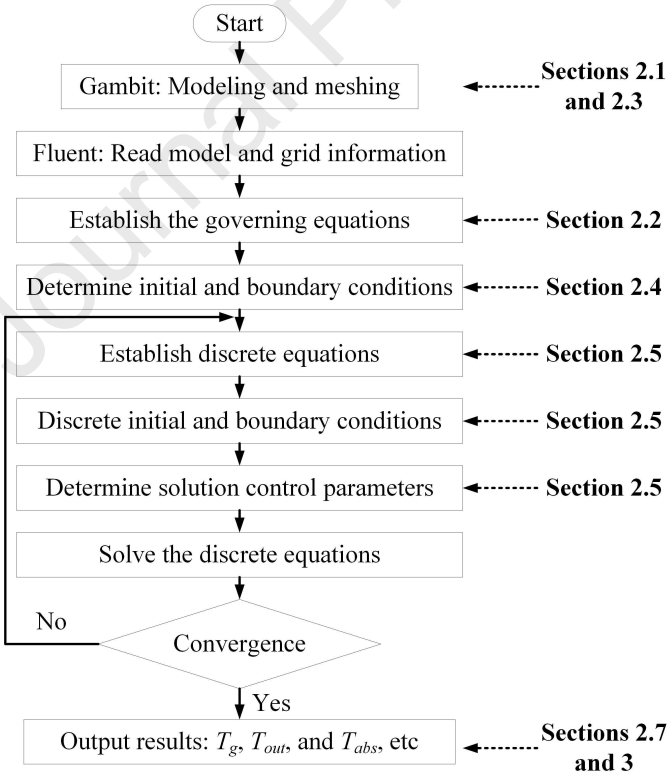

Fig. 6 Flow chart of the numerical modeling program

2.5 Simulation procedures

Calculations reported hereafter have been performed on the general purpose

commercial steady state ANSYS Fluent 17.0 by using the finite volume method. A body force weighted scheme was utilized using the SIMPLE algorithm for pressure velocity coupling discretization to obtain the solution. The momentum, energy, and continuity equations in the numerical simulations were discretized with a second-order upwind scheme. The minimum convergence criteria for the continuity, momentum, energy, and radiation equations were 10^{-3}, 10^{-3}, 10^{-6}, and 10^{-3}, respectively. **Fig. 6** shows the flow chart of the program.

2.6 Data processing

The performance parameters of FPSAC, such as thermal collection power, heat loss, and instantaneous efficiency, should be solved and analyzed under different working conditions. Under steady-state conditions, the energy balance equation of FPSAC is as follows:

$$Q_{total}=A_gI=Q_{coll}+Q_{loss}\,, \tag{15}$$

where

$$Q_{loss}=Q_{ac-amb}+Q_{bp-amb}+Q_{con,g-amb}+Q_{r,g-sky}\,, \tag{16}$$

$$Q_{ac-amb}=h_{ac-amb}A_{ac}\left(T_{ac}-T_{amb}\right), \tag{17}$$

$$Q_{bp-amb}=h_{bp-amb}A_{bp}\left(T_{bp}-T_{amb}\right), \tag{18}$$

$$Q_{con,g-amb}=h_{g-amb}A_g\left(T_g-T_{amb}\right), \tag{19}$$

$$Q_{r,g-sky}=A_g\cdot\varepsilon_g\cdot\sigma\cdot\left(\left(T_g+273.15\right)^4-\left(T_{sky}^*+273.15\right)^4\right), \tag{20}$$

where $h_{ac\text{-}amb}$, $h_{bp\text{-}amb}$, $h_{g\text{-}amb}$, and T_{sky}^* can be calculated using Eqs. (11) and (12), A_g, A_{ac}, and A_{bp} are the outer surface areas of glass, air channel, and back plate, respectively (m^2), ε_g is the emissivity of glass (0.85), and σ is the Stefan Boltzmann constant (5.67×10^{-8} W/($m^2\cdot K^4$)), T_g, T_{ac}, T_{bp}, and T_{amb} are the temperatures of glass, air channel, back plate, and ambient, respectively (°C).

The instantaneous efficiency of the collector is used to investigate the performance of the collector at a certain moment in real time. Its definition is as follows [9]:

$$\eta_{coll} = \frac{Q_{coll}}{A_g I} = F' \left(\eta_0 - U_L \frac{T_m - T_{amb}}{I} \right), \quad (21)$$

$$\eta_0 = \left(\alpha_{abs} \cdot \gamma_g \right)_e = 1.02 \cdot \alpha_{abs} \cdot \gamma_g , \quad (22)$$

where *F'* is the efficiency factor of the collector, γ_g and α_{abs} represent the transmissivity of the glazing and absorptivity of the absorber, respectively, η_0 is the optical efficiency of FPSAC, U_L is the total heat loss coefficient of the collector, and T_m is the average temperature of the HTA (T_{in}+T_{out})/2 (°C).

2.7 Validation of simulation results

In this study, the experimental data in a relatively stable period of time were selected to verify the numerical model. **Fig. 7** reveals the influence of the number of grids on the numerical simulation results to verify the accuracy of grid division method and calculation results. The average solar irradiance is 813 W/m^2, the outdoor wind velocity is 0.70 m/s, the inlet temperature of FPSAC is 16.50 °C, the volume flow rate of HTA is 120 m^3/h, and the ambient temperature is 5.25 °C. In the case of adjusting the node spacing, 5 groups of grids are generated, and the element numbers are 791,866, 985,474, 1,206,488, 1,564,368 and 1,736,325. The outlet temperature of FPSAC decreases first with the increase in the number of elements (decreasing the distance between nodes) and then stabilizes when the number of elements is 1,564,368. Therefore, a grid number of 1,564,368 was selected to accelerate the calculation while ensuring the accuracy.

Fig. 8 demonstrates the comparison results of numerical simulation and experiment. Twenty sets of experimental data with constant inlet temperature were selected to verify the reliability of the numerical model. The volume flow rate of the HTA in all experiments is 120 m^3/h. The range of error between the experiment and simulation is ±5.0%. Therefore, the numerical model is reliable and can predict the heat transfer characteristics of FPSAC.

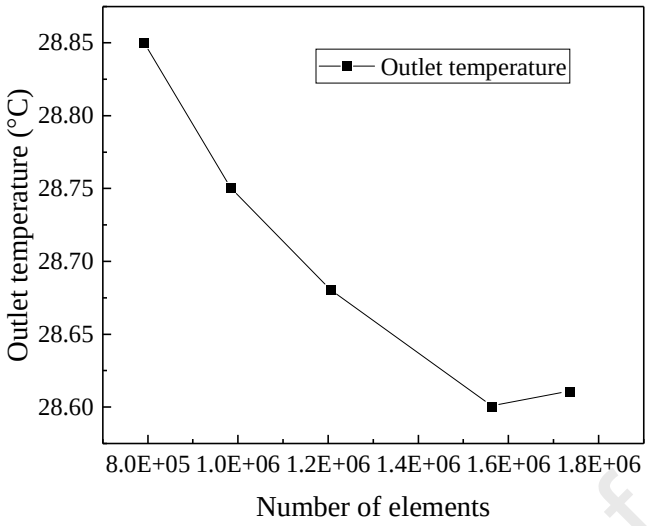

Fig. 7 Grid independence test for the numerical model

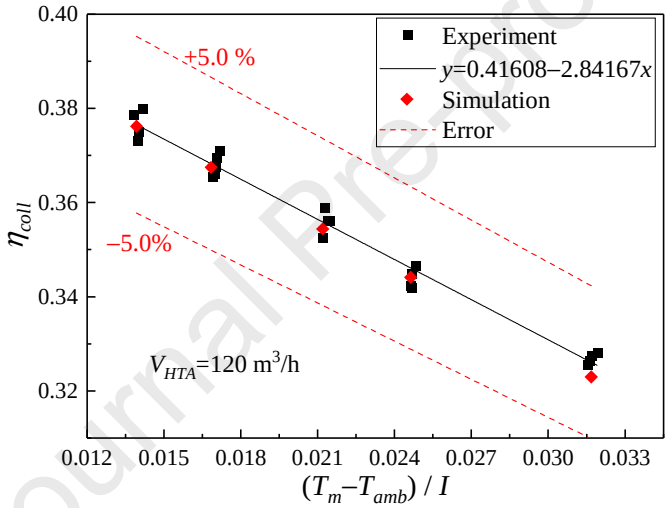

Fig. 8 Comparison of experimental and simulation results

2.8 Numerical model of four FPSACs with different glass covers

Four different models of FPSACs were established and numerically studied to reduce the heat loss at the top of the glass cover. The structure of the four FPSAC models is the same, except for the glass cover types. **Fig. 9** illustrates a schematic of the glazing types in the four models.

For Model 1 (original model): A single glazing with a thickness of 3 mm is used to cover the top of the FPSAC for reducing the heat loss on the top.

For Model 2: A double glazing filled with air is used to cover the top of the FPSAC. Relevant studies have shown that for double glazing with air and argon as the filling medium, the heat transfer coefficient of double glazing is smaller when the

distance between the two glasses is 12–13 mm. If the distance continues to increase, then the heat transfer coefficient no longer changes considerably [34]. The current study selects 12 mm as the distance between the two glasses. The material and thickness of each glasses are the same as Model 1.

For Model 3: A double glazing filled with argon is used to cover the top of the FPSAC. The distance between the two glasses is selected to be 12 mm [34]. The material and thickness of each glasses are the same as Model 1.

For Model 4: A vacuum glass is used to cover the top of the FPSAC. Considering the pressure bearing capacity of glass, the distance between the two glasses is 0.1–0.2 mm [33], and 0.15 mm is used in this study. The pillar inside the vacuum glass is disregarded in the model. The material and thickness of each glasses are the same as Model 1.

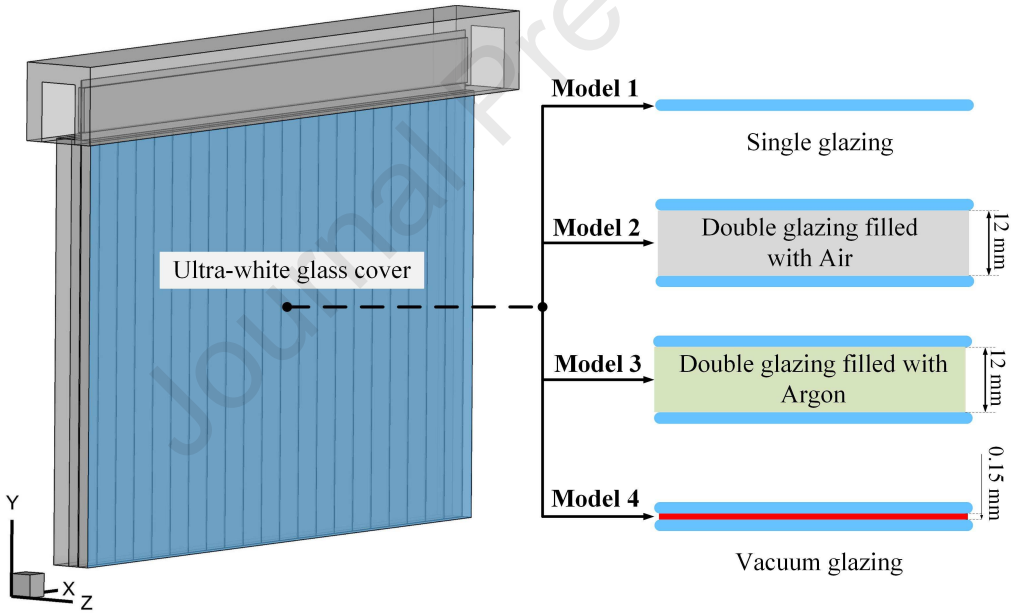

Fig. 9 Schematic of glass cover for four different models

The physical or optical properties of air, argon, vacuum, and glass materials are shown in **Tables 2** and **3**. The physical properties of the thin air in the vacuum layer are calculated in accordance with the following equations [33].

$$\lambda_{va} = \frac{\lambda_{air}}{1 + \frac{\left(1.07\times10^{-7}\right)\left(T_{va} + 273.15\right)}{\delta_{va} P_{va}}}, \tag{23}$$

$$P_{va}M = \rho_{va}R'\left(T_{va} + 273.15\right), \tag{24}$$

where λ_{va}, δ_{va}, T_{va}, ρ_{va}, and P_{va} are the thermal conductivity, thickness, temperature, density, and absolute pressure (10 Pa) of the medium in vacuum layer, M is the molar mass of air, and R' is a constant (approximately 8.314 J/(mol·K)).

3. Results and discussion

3.1 Influence of ambient temperature on the performance of four FPSACs

This section investigates the thermal performance of four FPSACs at different ambient temperatures. The solar irradiance is 891.7 W/m^2, the outdoor wind velocity is 0.65 m/s, the inlet temperature of FPSAC is 50 °C, the volume flow rate of HTA is 120 m^3/h, and the ambient temperature is from −20 °C to 40 °C.

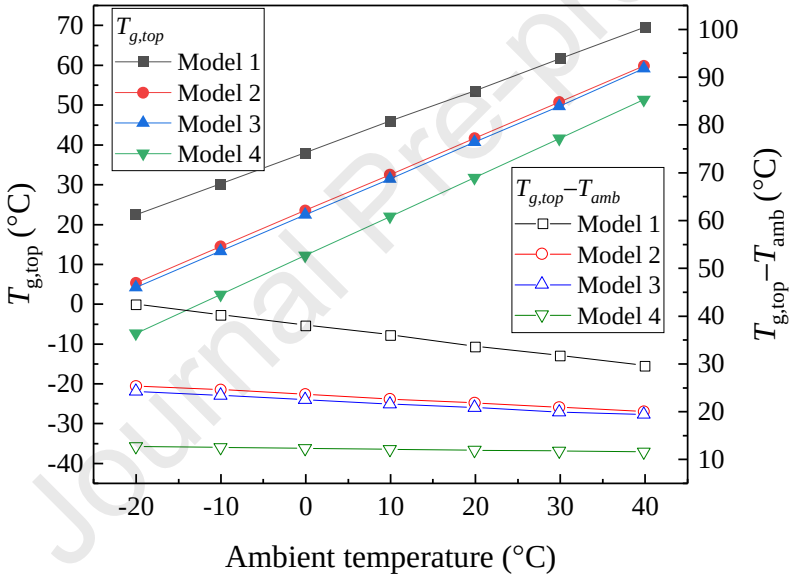

Fig. 10 Curve of $T_{g,top}$ and $T_{g,top}$–T_{amb} of the four models with the ambient temperature.

The temperature and heat loss at the top glazing are directly related to the thermal performance of the FPSAC. **Fig. 10** demonstrates the curves of the top glazing temperature ($T_{g,top}$) and the temperature difference between the top glazing and the ambient temperature ($T_{g,top}$–T_{amb}) of four models with the ambient temperature (T_{amb}). The $T_{g,top}$ of all models increases, and $T_{g,top}$–T_{amb} gradually attenuates with the increase in T_{amb}. When T_{amb} changes from −20 °C to 40 °C, the ranges of $T_{g,top}$–T_{amb} of Models 1, 2, 3, and 4 are 29.54 °C–42.36 °C, 19.84 °C–25.17 °C, 19.21 °C– 24.06 °C, and 11.37 °C–12.46 °C, respectively. In

terms of $T_{g,top}$–T_{amb}, Model 1>Model 2>Model 3>Model 4. The use of double glazing increases the overall heat transfer resistance of the glass cover (R_g). Thus, the thermal insulation performance of double glazing on the top of the collector is better, especially the vacuum glazing in Model 4 has the least sensitivity to T_{amb}. The thermal conductivities of air (Model 2) and argon (Model 3) are of the same order of magnitude. The difference in performance between the two collectors is relatively small [42].

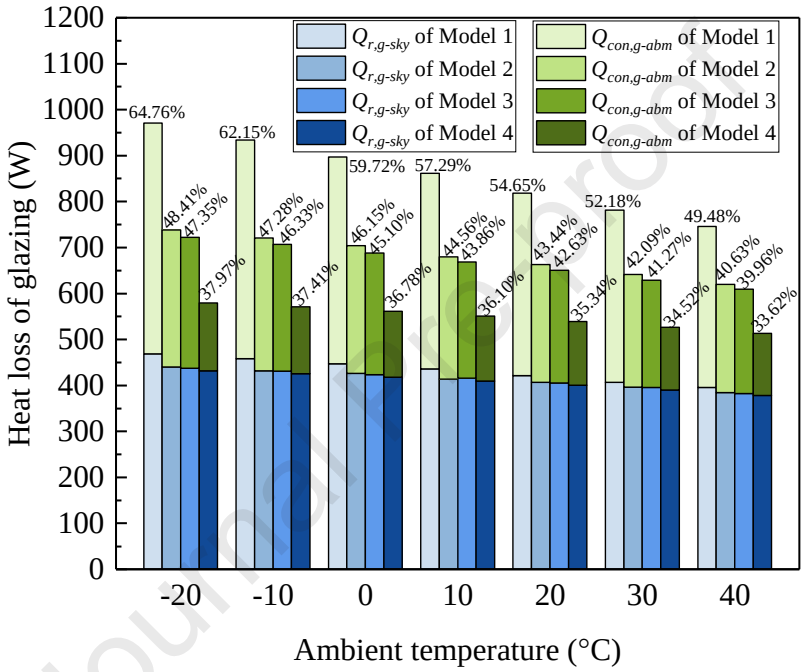

Fig. 11 Column of the top glazing heat loss of the four models at different ambient temperatures

Fig. 11 represents the heat loss of the top glazing of the four models at different ambient temperatures (T_{amb}), including convective heat loss ($Q_{con,g\text{-}amb}$) and radiant heat loss ($Q_{r,g\text{-}sky}$). The ratio of the total heat loss of the top glazing ($Q_{g,total}$ = $Q_{con,g\text{-}amb}$+$Q_{r,g\text{-}sky}$) to the total input solar radiation (A_gI) is shown in the upper part of the column. The $Q_{g,total}$ of the four models decreases with the increase in T_{amb}. When T_{amb} changes from −20 °C to 40 °C, the ranges of $Q_{g,total}/A_gI$ for Models 1, 2, 3, and 4 are 48.48%–64.76%, 48.48%–64.76%, 39.96%–47.35%, and 33.62%–37.97%, respectively. $Q_{r,g\text{-}sky}$ appears to be stable for all four models. With the increase in T_{amb}, the total heat loss of the top glazing is greatly reduced, but the main part of the reduction is $Q_{con,g\text{-}amb}$. The $Q_{r,g\text{-}sky}$ of the top glazing in Models 2, 3, and 4 is greater

than $Q_{con,g\text{-}amb}$. The high emissivity (0.85) of ultra white glass used in these FPSACs is the main reason for this phenomenon. Thin films characterized with high transmittance and low emissivity may be an option for reducing $Q_{r,g\text{-}sky}$.

Fig. 12 illustrates the effect of different ambient temperatures (T_{amb}) on the absorber temperature (T_{abs}) and outlet temperature (T_{out}) of four different FPSACs. T_{abs} and T_{out} are the two most intuitive parameters that represent the thermal performance of an FPSAC. A high T_{abs} indicates that an FPSAC has good heat insulation performance to a certain extent, and T_{out} directly determines the energy grade that the target can obtain. T_{abs} and T_{out} of all FPSACs increase with the increase in T_{amb}. Under the same meteorological and boundary conditions, the FPSACs with double glazing (Models 2, 3, and 4) have higher T_{abs} and T_{out} than the FPSAC with single glazing (Model 1). Although double glazing reduces the solar radiation projected to the absorber (**Table 4**), its good thermal insulation performance greatly reduces the temperature of the top glazing (**Fig. 10**). Thus, the glazing heat loss is greatly reduced (**Fig. 11**). When T_{amb} changes from −20 °C to 40 °C, the T_{out} ranges of Models 1, 2, 3 and 4 are 57.04 °C–64.72 °C, 61.30 °C –66.01 °C, 61.73 °C–66.32 °C, and 65.36 °C–68.79 °C, respectively.

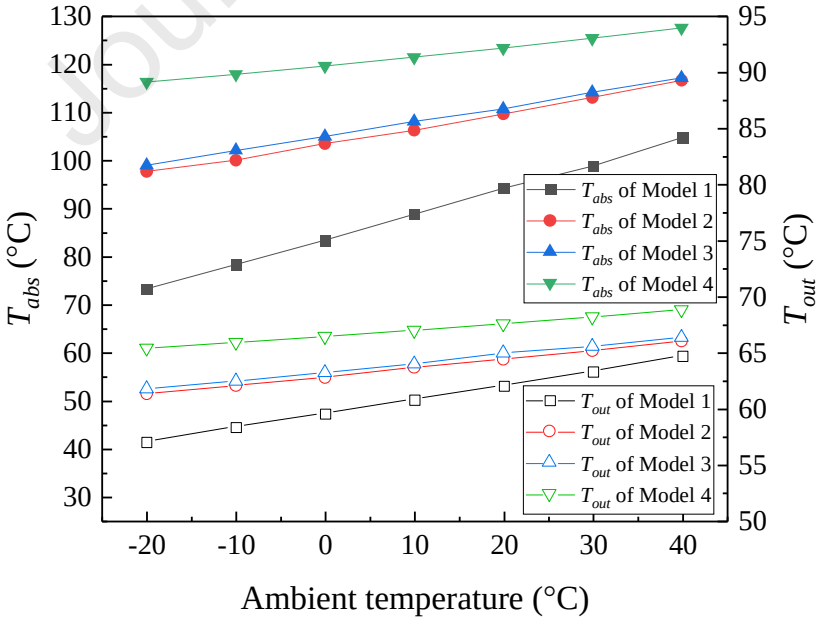

Fig. 12 Curves of absorber temperature (T_{abs}) and outlet temperature (T_{out}) of the four FPSACs at different ambient temperatures (T_{amb})

Fig. 13 shows the efficiency curve of the four models at different ambient temperatures (T_{amb}). T_{amb} greatly affects the thermal efficiency (η_{coll}) of the four FPSACs. The increase in T_{amb} helps to increase the η_{coll} of all collectors. The order of η_{coll} is $\eta_{coll,Model\ 1} < \eta_{coll,Model\ 2} < \eta_{coll,Model\ 3} < \eta_{coll,Model\ 4}$ by comparing the four models. When T_{amb} changes from −20 °C to 40 °C, the ranges of η_{coll} of Models 1, 2, 3, and 4 are 17.20%–35.83%, 26.90%–38.19%, 27.90%–38.83%, and 36.55%–44.73%, respectively. The inlet temperature of the four FPSACs is the same, which is 50 °C. Model 4 with vacuum glazing has excellent thermal performance at different T_{amb}, especially in low-temperature environments.

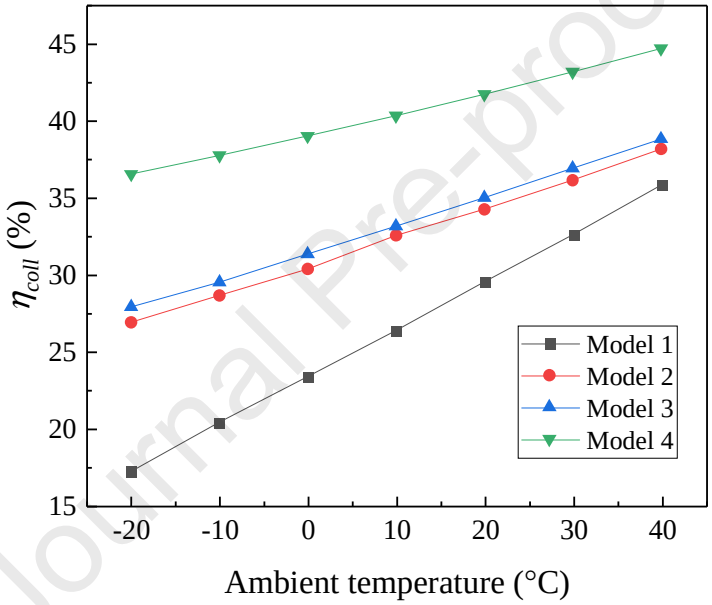

Fig. 13 Efficiency curve of the four models at different ambient temperatures

3.2 Influence of inlet temperature on the performance of four FPSACs

This section investigates the thermal performance of four FPSACs at different inlet temperatures. The solar irradiance is 891.7 W/m^2, the outdoor wind velocity is 0.65 m/s, the ambient temperature (T_{amb}) is −10 °C, the volume flow rate of HTA is 120 m^3/h, and the inlet temperature of FPSACs is from 35 °C to 65 °C.

Fig. 14 demonstrates the curve of the top glazing temperature ($T_{g,top}$) and the down glazing temperature ($T_{g,down}$) of four models with the inlet temperature (T_{in}). “Top” and “Down” indicate the side of the double glazing that is in contact with the environment and the side close to the absorber, respectively. When T_{amb} is −10 °C, the

influence of the change in T_{in} on the top glazing temperature is relatively small. When the inlet temperature increases from 35 °C to 65 °C, the temperature increases in the top glazing of Models 1, 2, 3, and 4 are 5.03 °C, 2.31 °C, 1.86 °C, and 0.41 °C, respectively. The order of $T_{g,\,top}$ is $T_{g,\,top,\,Model\,1} > T_{g,\,top,Model\,2} > T_{g,\,top,Model\,3} > T_{g,\,top,Model\,4}$ by comparing the four models. Conducting heat from the down glass to the top glass is difficult because the double glazing increases the overall thermal resistance of the glass cover (R_g). The top glazing temperature of Model 4 (vacuum glass) is stable between 2.07 °C and 2.48 °C when T_{in} changes between 35 °C and 65 °C. The down glazing temperature of Models 2, 3, and 4 shows an opposite trend: $T_{g,\,down,\,Model\,2} < T_{g,\,down,\,Model\,3} < T_{g,\,down,\,Model\,4}$. The insulation performance of vacuum glass is proven.

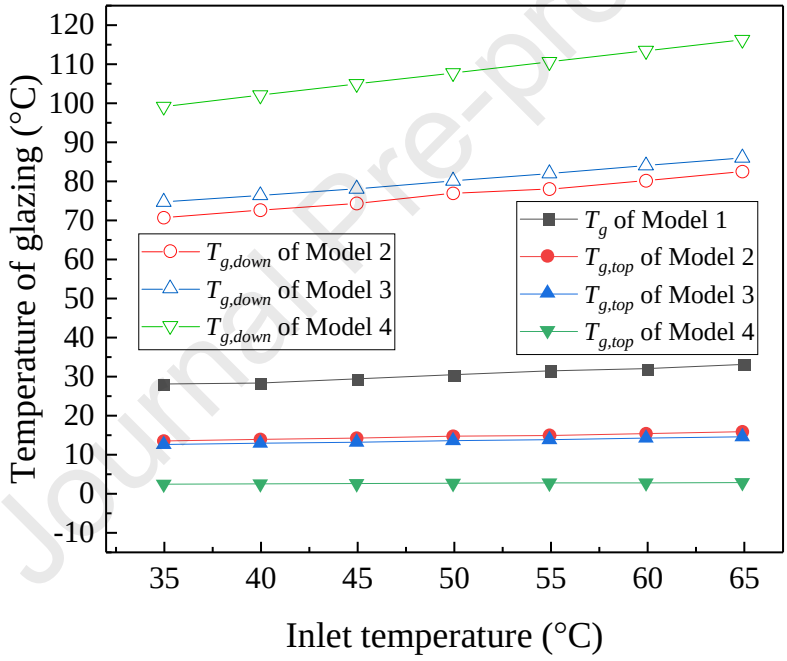

Fig. 14 Curve of $T_{g,top}$ and $T_{g,down}$ of the four models with the inlet temperature of FPSAC

Fig. 15 represents the heat loss of the top glazing of the four models at different inlet temperatures (T_{in}), including convective heat loss ($Q_{con,g\text{-}amb}$) and radiant heat loss ($Q_{r,g\text{-}sky}$). The ratio of the total heat loss of the glazing ($Q_{g,total} = Q_{con,g\text{-}amb}+Q_{r,g\text{-}sky}$) to the input solar radiation (A_gI) is shown in the upper part of the column. Increasing T_{in} increases $Q_{g,total}$ of the four models. $Q_{g,total}$ is closely related to the top glazing temperature. With reference to **Fig. 14**, the order of $Q_{g,total}$ of the four models is as follows: $Q_{g,total,Model\,1} > Q_{g,total,Model\,2} > Q_{g,total,Model\,3} > Q_{g,total,Model\,4}$. When T_{in} changes

from 35 °C to 65 °C, the ranges of $Q_{g,total}/A_gI$ for Models 1, 2, 3, and 4 are 57.52%–66.13%, 44.32%–50.86%, 43.60%–49.75%, and 34.92%–40.45%, respectively. Compared with Model 1, the heat loss rate of the top glazing of Models 2, 3, and 4 is reduced by 15.27%, 16.38%, and 25.68% at the maximum.

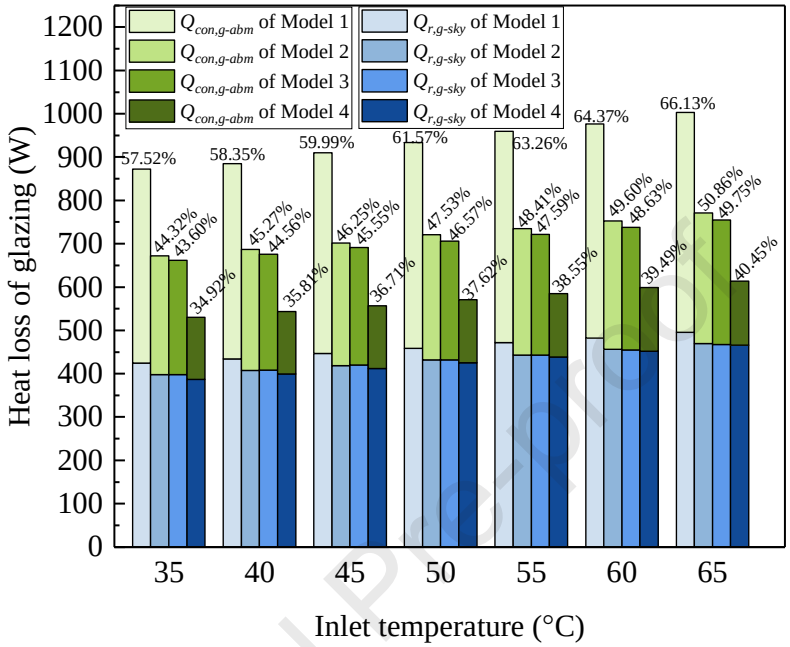

Fig. 15 Column of the top glazing heat loss of the four models at different inlet temperatures

Fig. 16 illustrates the effect of different inlet temperatures (T_{in}) on the absorber temperature (T_{abs}) and outlet temperature (T_{out}) of four different FPSACs. T_{abs} and T_{out} of the four models increase with the increase in T_{in}. T_{abs} is a main factor affecting the heat gain performance of HTA. In the case of the same T_{in}, Models 2, 3, and 4 with double glazing have higher T_{abs} and T_{out} than Model 1 with single glazing. When T_{in} is 65 °C, T_{abs} and T_{out} of Model 4 reach the highest values of 127.25 °C and 79.99 °C, which are 42.70 °C and 8.89 °C higher than Model 1. When T_{in} increases from 35 °C to 65 °C, the ranges of the inlet and outlet temperature differences of Models 1, 2, 3 and 4 are 6.10 °C–10.31 °C, 10.28 °C–13.68 °C, 10.75 °C–14.00 °C, and 14.99 °C–17.34 °C, respectively.

Fig. 17 shows the efficiency curve (η_{coll}) of the four models at different inlet temperatures (T_{in}). Under other same conditions, increasing the T_{in} of FPSAC reduces its efficiency. The efficiency of Model 1 is significantly lower than that of Models 2, 3,

and 4. When T_{in} changes from 35 °C to 65 °C, the ranges of η_{coll} of Models 1, 2, 3, and 4 are 14.90%–25.18%, 24.53%–32.58%, 25.59%–33.27%, and 34.11%–41.26%, respectively. Model 4 with vacuum glazing shows good thermal performance.

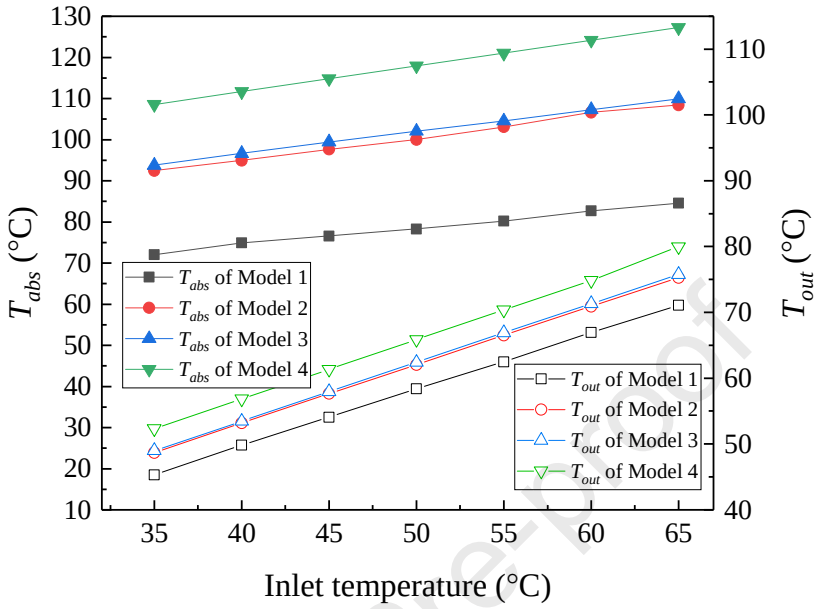

Fig. 16 Curves of absorber temperature (T_{abs}) and outlet temperature (T_{out}) of the four FPSACs at different inlet temperatures (T_{in})

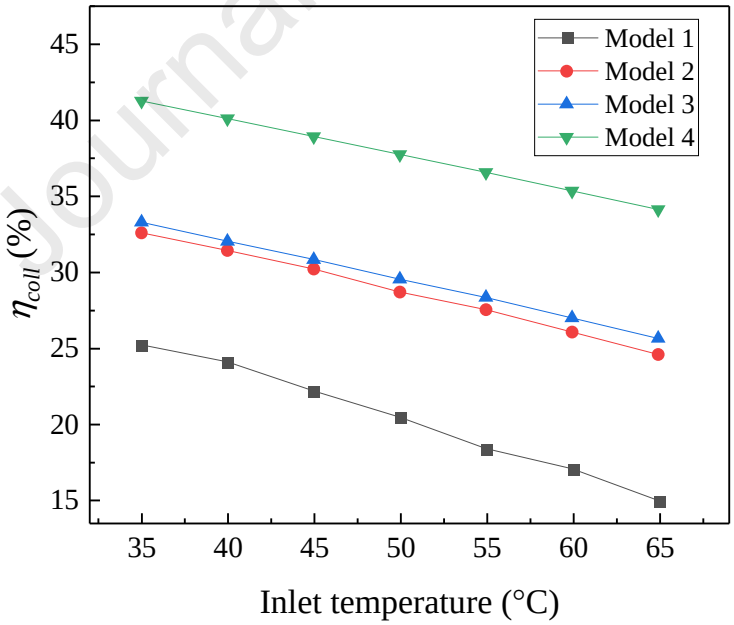

Fig. 17 Efficiency curve of the four models at different inlet temperatures (T_{in})

3.3 Influence of volume flow rate on the performance of four FPSACs

This section investigates the heat transfer performance of four FPSACs at different volume flow rates. The solar irradiance is 891.7 W/m^2, the outdoor wind

velocity is 0.65 m/s, the ambient temperature (T_{amb}) is −10 °C, the inlet temperature (T_{in}) of FPSACs is 50 °C, and the volume flow rates of HTA are from 30 m^3/h to 210 m^3/h.

Fig. 18 demonstrates the curve of the top glazing temperature ($T_{g,top}$) and the down glazing temperature ($T_{g,down}$) of four models with the volume flow rate (V_{HTA}). V_{HTA} has no obvious influence on $T_{g,top}$ and $T_{g,down}$ of the four models, especially after V_{HTA} reaches 120–150 m^3/h. The $T_{g,top}$ of the four models is stable at around 30.47 °C, 14.56 °C, 13.42 °C, and 2.33 °C, respectively, after V_{HTA} increases to 150 m^3/h. When V_{HTA} increases to 150 m^3/h, the value of $T_{g,down}$ in Models 2, 3, and 4 is stable at 74.82 °C, 78.30 °C, and 108.09 °C, respectively.

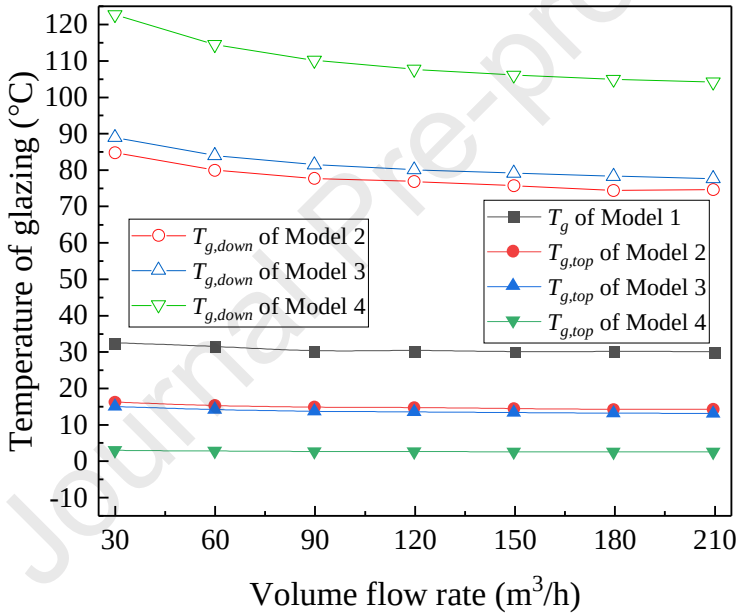

Fig. 18 Curve of $T_{g,top}$ and $T_{g,down}$ of the four models with the volume flow rate

Fig. 19 represents the heat loss of the top glazing of the four models at different volume flow rates (V_{HTA}), including convective heat loss ($Q_{con,g\text{-}amb}$) and radiant heat loss ($Q_{r,g\text{-}sky}$). The ratio of the total heat loss of the glazing ($Q_{g,total} = Q_{con,g\text{-}amb}+Q_{r,g\text{-}sky}$) to the input solar radiation (A_gI) is shown in the upper part of the column. **Fig. 18** reflects $Q_{g,total}$ to a certain extent. The top glazing temperature of the four models does not change significantly with the increase in V_{HTA}. **Fig. 19** illustrates the most intuitive data. When V_{HTA} changes from 30 m^3/h to 210 m^3/h, the ranges of $Q_{g,total}/A_gI$ for Models 1, 2, 3, and 4 are 61.50%–66.73%, 46.09%–52.17%, 45.17%–51.20%, and

36.12%–42.94%, respectively. The reduction of convection heat transfer is still the main means to reduce $Q_{g,total}$ by comparing the four models.

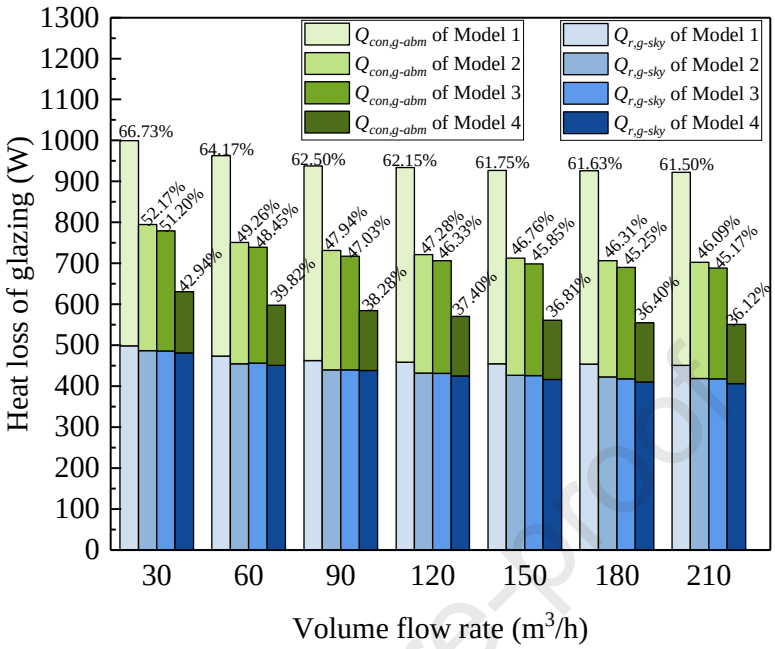

Fig. 19 Column of the top glazing heat loss of the four models at different volume flow rates

Fig. 20 illustrates the effect of different volume flow rates (V_{HTA}) on the absorber temperature (T_{abs}) and the temperature difference between the inlet and outlet (ΔT) of four different FPSACs. The value of T_{abs} of all models gradually decreases with the increase in V_{HTA}. The value of ΔT in all models gradually decreases when V_{HTA} is increased. The decrease in the residence time of HTA per unit volume in the air channel is the main reason for this phenomenon. Similarly, this phenomenon becomes insignificant after V_{HTA} increases to 120–150 m^3/h. When V_{HTA} increases from 30 m^3/h to 210 m^3/h, the ranges of ΔT of Models 1, 2, 3 and 4 are 4.95 °C–23.36 °C, 7.24 °C–34.61 °C, 7.44 °C –38.60 °C, and 9.48 °C–46.10 °C, respectively. The small HTA volume flow rate helps to increase the outlet temperature of FPSACs.

Fig. 21 shows the efficiency (η_{coll}) curve of the four models at different volume flow rates (V_{HTA}). Combining the above analysis and **Fig. 21**, increasing the value of V_{HTA} increases η_{coll} to a certain extent. However, increasing η_{coll} by increasing V_{HTA} infinitely is unrealistic/uneconomical. When V_{HTA} increases to 150 m^3/h, the value of η_{coll} in the four models is stable at approximately 21.01%, 29.69%, 30.57%, and

38.92%, respectively.

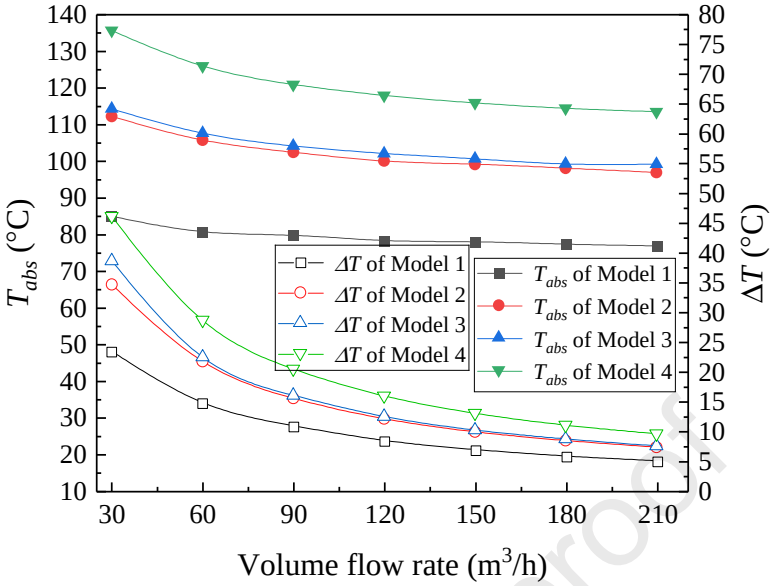

Fig. 20 Curves of absorber temperature (T_{abs}) and the temperature difference between the inlet and outlet (ΔT) of four FPSACs at different volume flow rates (V_{HTA})

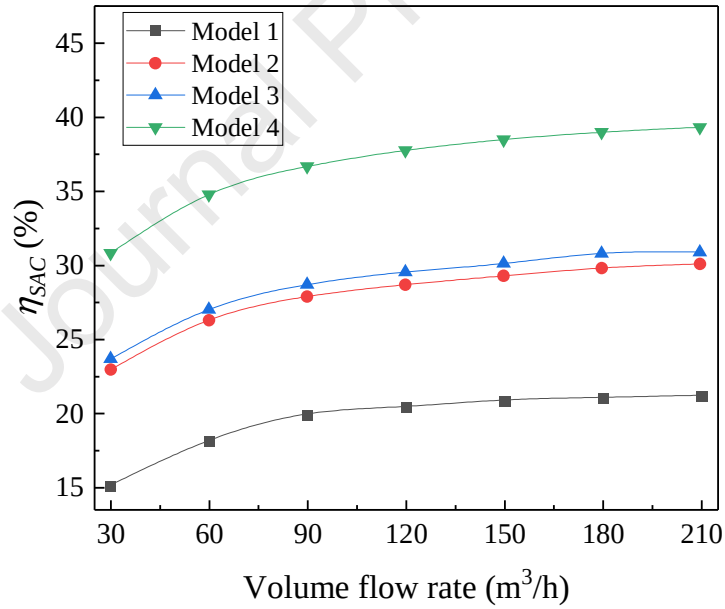

Fig. 21 Efficiency curve of the four models at different volume flow rates (V_{HTA})

3.4 Instantaneous efficiency curve of four FPSACs

The efficiency factor (F'), optical efficiency (η_0), and total heat loss coefficient (U_L) can comprehensively describe the structure and thermal performance of a collector. **Fig. 22** demonstrates the normalized efficiency curves of the four collectors. **Table 4** shows the details of the performance parameters of each FPSAC. The

intercept and slope of the normalized curve are $F'\cdot\eta_0$ and $F'\cdot U_L$, respectively (**Eq. (21)**). The maximum efficiencies that can be achieved for Models 1, 2, 3, and 4 under the operating condition of V_{HTA}=120 m^3/h are 41.794%, 42.304%, 42.846%, and 48.182%, respectively. Comparing the values of $F'\cdot U_L$ or U_L of the four models, their insulation conditions are as follows: Model 1 < Model 2 < Model 3 < Model 4 even if double glazing reduces the FPSAC's η_0. Compared with single glazing FPSAC (Model 1), double glazing (especially vacuum glass) FPSAC exhibits excellent thermal performance when the cycle temperature of HTA is higher.

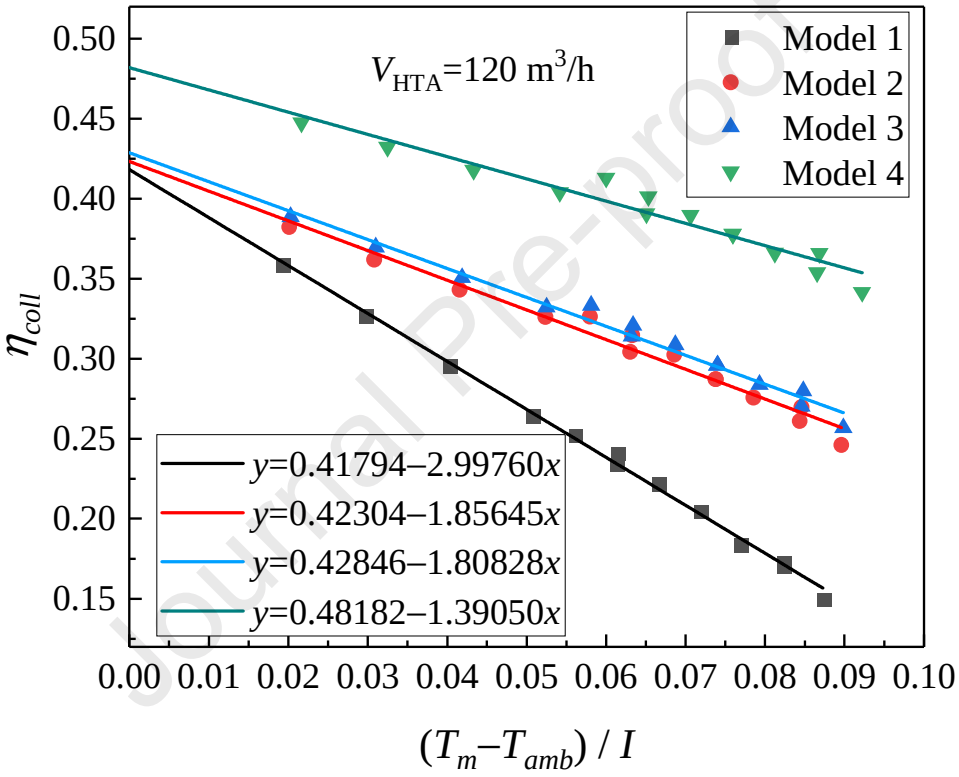

Fig. 22 Normalized curves of the four models

Table 4 Comparison of performance parameters of the four models

Item	$\alpha_{abs}\gamma_g$	$(\alpha_{abs}\gamma_g)_e$ or η_0	F'	U_L
Model 1	0.84630	0.86323	0.48416	6.19133
Model 2	0.75330	0.76837	0.55057	3.37186
Model 3	0.75330	0.76837	0.55762	3.24283
Model 4	0.75330	0.76837	0.62707	2.21745

4 Conclusion

Double glazing FPSACs were proposed in this study to improve the thermal performance of FPSAC at low ambient temperature and high inlet temperature. The thermal performance of different types of double glazing FPSAC was evaluated at low ambient temperature and high inlet temperature through numerical simulation, and the results were compared with single glazing FPSAC. The reliability of the numerical model was verified. Four numerical models, namely, single glazing FPSAC (Model 1), double glazing filled with air FPSAC (Model 2), double glazing filled with argon FPSAC (Model 3), and vacuum glazing FPSAC (Model 4), were established. The thermal performance of the four models under different ambient temperatures, different inlet temperatures, and different HTA volume flow rates was studied and compared. The main conclusions are as follows:

1. Compared with Model 1, Models 2, 3, and 4 have higher thermal performance (mainly outlet temperature and efficiency) at low ambient temperature and high inlet temperature. When the inlet temperature of the collector is 50 °C and ambient temperature changes from −20 °C to 40 °C, the ranges of outlet temperature of Models 1, 2, 3, and 4 are 57.04 °C–64.72 °C, 61.30 °C–66.01 °C, 61.73 °C –66.32 °C, and 65.36 °C–68.79 °C, respectively. Correspondingly, the ranges of η_{coll} of Models 1, 2, 3, and 4 are 17.20%–35.83%, 26.90%–38.19%, 27.90%–38.83%, and 36.55%–44.73%, respectively.

2. The HTA volume flow rate (V_{HTA}) has a limited effect on the thermal efficiency of all models. When the inlet temperature of the collector is 50 °C, the ambient temperature is −10 °C, and V_{HTA} increases to 150 m^3/h, the values of η_{coll} in the Models 1, 2, 3, and 4 are stable at approximately 21.01%, 29.69%, 30.57%, and 38.92%, respectively.

3. Compared with Model 1, Models 2, 3, and 4, have relatively higher efficiency factor (F') and lower total heat loss coefficient (U_L). When the V_{HTA} of the collector is 120 m^3/h, the F' and U_L of Models 1, 2, 3, and 4 are 0.48416 and 6.19133, 0.55057 and 3.37186, 0.55762 and 3.24283, 0.62707 and 2.21745, respectively.

Acknowledgements

The authors gratefully acknowledge the financial support provided by Beijing Municipal Natural Science Foundation (Grant No.3192009), National Natural Science Foundation of China (Grant No.51906177) and Natural Science Foundation of Tianjin city of China (Grant No. 18JCQNJC77400).

References

[1] Z. Badiei, M. Eslami, K. Jafarpur. Performance improvements in solar flat plate collectors by integrating with phase change materials and fins: A CFD modeling. Energy 2020; 192:116719.

[2] Jie Deng, Tadhg S. O'Donovan, Zhiyong Tian, Josh King, Stuart Speake. Thermal performance predictions and tests of a novel type of flat plate solar thermal collectors by integrating with a freeze tolerance solution. Energy Conversion and Management 2019; 198:111784.

[3] Evangelos Bellos, Christos Tzivanidis. Performance analysis and optimization of an absorption chiller driven by nanofluid based solar flat plate collector. Journal of Cleaner Production 2018; 174:256-272.

[4] Xueling Li, Huawei Chang, Lijian Zeng, Xiaorong Huang, Yichao Li, Renfu Li, Zhaojun Xi. Numerical analysis of photothermal conversion performance of MXene nanofluid in direct absorption solar collectors. Energy Conversion and Management 2020; 226:113515.

[5] Jorge Facão. Optimization of flow distribution in flat plate solar thermal collectors with riser and header arrangements. Solar Energy 2015; 120:104-112.

[6] Jingyu Wang, Jian Yang, Zhilong Cheng, Yan Liu, Yitung Chen, Qiuwang Wang. Experimental and numerical study on pressure drop and heat transfer performance of grille-sphere composite structured packed bed. Applied Energy 2018; 227:719-730.

[7] Dongwei Zhang, Hanzhong Tao, Mimi Wang, Zishuai Sun, Chuan Jiang. Numerical simulation investigation on thermal performance of heat pipe flat-plate solar collector. Applied Thermal Engineering 2017; 113-126.

[8] Abdellah Shafieian, Mehdi Khiadani, Atallah Nosrati. A review of latest developments, progress, and applications of heat pipe solar collectors. Renewable and Sustainable Energy Reviews 2018; 95:273-304.

[9] Sebastian Müller, Federico Giovannetti, Rolf Reineke-Koch, Oliver Kastner, Bernd Hafner. Simulation study on the efficiency of thermochromic absorber coatings for solar thermal flat-plate collectors. Solar Energy 2019; 865-874.

[10] A.A. El-Sebaii, H. Al-Snani. Effect of selective coating on thermal performance of flat plate solar air heaters. Energy 2010; 35:1820-1828.

[11] P. Konttinen, P.D. Lind. Microstructural optimization and extended durability studies of low-cost rough graphite–aluminium solar absorber surfaces. Renewable Energy 2004; 29:823-839.

[12] Alison Subiantoro, Ooi Kim Tiow. Analytical models for the computation and optimization of single and double glazing flat plate solar collectors with normal and small air gap spacing. Applied Energy 2013; 104:392-399.

[13] F.P. Incropera, D.P. DeWitt, T.L. Bergman, A.S. Lavine. Fundamentals of Heat and Mass Transfer. 2006.

[14] F. Giovannetti, S. Föste, N. Ehrmann, G. Rockendorf. High transmittance, low emissivity glass covers for flat plate collectors: Applications and performance. Solar Energy 2014; 104:52-59.

[15] N. Ehrmann, R. Reineke-Koch, S. Föste, F. Giovannetti. The influence of process parameters and coating properties of double glazing coated with transparent conducting oxides on the efficiency of solar-thermal flat-plate collectors. Thin Solid Films 2013; 532:132-140.

[16] S. Farahat, F. Sarhaddi, H. Ajam. Exergetic optimization of flat plate solar collectors. Renewable Energy 2009; 34:1169-1174.

[17] Liqun Zhou, Yiping Wang, Qunwu Huang. CFD investigation of a new flat plate collector with additional front side transparent insulation for use in cold regions. Renewable Energy 2019; 138:754-763.

[18] Ramadhanl Bakari, Rwaichi J. A. Minja, Karoli N. Njau. Effect of Glass

Thickness on Performance of Flat Plate Solar Collectors for Fruits Drying. Journal of Energy 2014; 2014:247287.

[19] Roberto Baccoli, Andrea Frattolillo, Costantino Mastino, Sebastiano Curreli, Emilio Ghiani. A comprehensive optimization model for flat solar collector coupled with a flat booster bottom reflector based on an exact finite length simulation model. Energy Conversion and Management 2018; 164:482-507.

[20] H.M.S. Hussein, G.E. Ahmad, M.A. Mohamad. Optimization of operational and design parameters of plane reflector-tilted flat plate solar collector systems. Energy 2000; 25:529-542.

[21] Mauricio Carmona, Mario Palacio. Thermal modelling of a flat plate solar collector with latent heat storage validated with experimental data in outdoor conditions. Soar Energy 2019; 177:620-633.

[22] A.E. Kabeel, Gamal B. Abdelaziz, Emad M.S. El-Said. Experimental investigation of a solar still with composite material heat storage: Energy, exergy and economic analysis. Journal of Cleaner Production 2019; 231:21-34.

[23] Chuanqi Chen, Yanhua Diao, Yaohua Zhao, Zeyu Wang, Lin Liang, Tengyue Wang, Tingting Zhu, Cheng Ma. Thermal performance of a closed collector-storage solar air heating system with latent thermal storage: An experimental study. Energy 2020; 202:117764.

[24] Yanyi Sun, Yupeng Wu, Robin Wilson, Sixu Lu. Experimental measurement and numerical simulation of the thermal performance of a double glazing system with an interstitial Venetian blind. Building and environment 2016; 103:111-122.

[25] W.J. Hee, M.A. Alghoul, B.Bakhtyar, OmKalthum Elayeb, M.A. Shameri, M.S. Alrubaih, K. Sopian. The role of window glazing on daylighting and energy saving in buildings. Renewable and Sustainable Energy Reviews 2015; 42:323-343.

[26] Edward K. Summers, Mohammed A. Antar, John H. Lienhard V. Design and optimization of an air heating solar collector with integrated phase change material energy storage for use in humidification–dehumidification desalination. Solar Energy 2012; 86:3417-3429.

[27] R. C. Zheng. Civil building solar water heating system engineering technical manual 2011. China, Chemical Industry Press.

[28] M. Ammar, A. Mokni, H. Mhiri, P. Bournot. Numerical analysis of solar air collector provided with rows of rectangular fins. Energy Reports 2020; 6:3412-3424.

[29] M. R. Saffarian, M. Moravej, M. H. Doranehgard. Heat transfer enhancement in a flat plate solar collector with different flow path shapes using nanofluid. Renewable Energy 2020; 146: 2316-2329.

[30] Marilena Musto, Nicola Bianco, Giuseppe Rotondo, Flavio Toscano, Giuseppe Pezzella. A simplified methodology to simulate a heat exchanger in an aircraft's oil cooler by means of a Porous Media model. Applied Thermal Engineering 2016; 94: 836-845.

[31] Tingting Zhu, Yanhua Diao, Yaohua Zhao, Cheng Ma. Performance evaluation of a novel flat-plate solar air collector with micro-heat pipe arrays (MHPA). Applied Thermal Engineering 2017; 118:1-16.

[32] Tengyue Wang, Yaohua Zhao, Yanhua Diao, Ruyang Ren, Zeyu Wang. Performance of a new type of solar air collector with transparent-vacuum glass tube based on micro-heat pipe arrays. Energy 2019; 177:16-28.

[33] Ali Radwan, Takao Katsura, Saim Memon, Ahmed A. Serageldin, Makoto Nakamura, Katsunori Nagano. Thermal and electrical performances of semi-transparent photovoltaic glazing integrated with translucent vacuum insulation panel and vacuum glazing. Energy Conversion and Management 2020; 215:112920.

[34] 2001 ASHRAE Handbook, Fundamentals (SI), American Society of Heating, Refrigerating and Air-conditioning, Engineers, Inc., 1791 Tullie Circle, N.E., Atalanta, GA 30329.

Highlights

1. Different types of double glazings are applied into FPSAC.

2. The thermal performance of three double-glazing FPSACs is evaluated.

3. Vacuum-glazing FPSAC exhibits the best thermal performance.

Declaration of Interest Statement

The authors declare that they have no known competing financial interests or personal relationships that could have appeared to influence the work reported in this paper.